WILEY | Hindawi

Research Article

Reactive Transport Modelling of Elevated Dissolved Sulphide Concentrations in Sedimentary Basin Rocks

Mingliang Xie [ID],[1] **Danyang Su** [ID],[1] **Kerry T. B. MacQuarrie** [ID],[2] **and K. Ulrich Mayer** [ID][1]

[1]*Department of Earth, Ocean and Atmospheric Sciences, University of British Columbia, Canada*
[2]*Department of Civil Engineering, University of New Brunswick, Canada*

Correspondence should be addressed to Mingliang Xie; mxie@eoas.ubc.ca

Groundwater with total dissolved sulphide concentrations in excess of $1.0 \times 10^{-4}\,\mathrm{mol\,L^{-1}}$ ($3\,\mathrm{mg\,L^{-1}}$) is relatively common at intermediate depths in sedimentary basins. However, the mechanisms responsible for the formation and spatial distribution of these sulphidic waters in sedimentary basins, which have been affected by periods of glaciation and deglaciation, are not fully understood. Sulphate reduction rates depend on many factors including redox conditions, salinity, temperature, and the presence and abundance of sulphate, organic matter, and sulphate-reducing bacteria. Two-dimensional reactive transport modelling was undertaken to provide potential explanations for the presence and distribution of sulphidic waters in sedimentary basins, partially constrained by field data from the Michigan Basin underlying Southern Ontario, Canada. Simulations were able to generally reproduce the observed depth-dependent distribution of sulphide. Sulphate reduction was most significant at intermediate depths due to anoxic conditions and elevated sulphate concentrations in the presence of organic matter in waters with relatively low salinity. The simulations indicate that glaciation-deglaciation periods increase mixing of waters at this interfacial zone, thereby enhancing rates of sulphate reduction and the formation of sulphide. In addition, the simulations indicate that glaciation-deglaciation cycles do not significantly affect sulphide concentrations in low permeability units, even at shallow depths (e.g., 25 m), while concentrations in permeable units remain stable below depths of 500 m.

1. Introduction

Hydrogen sulphide (H_2S) is commonly found in organic-rich Palaeozoic sedimentary basins, such as the Michigan Basin (e.g., elevated sulphide concentrations have been observed at intermediate depths in southern Ontario, Canada [1–3]), the Gulf Coast Sedimentary Basin, USA [4], the Western Canadian Sedimentary Basin [5], and the Western Sichuan Basin, China [6], as well as in other organic-rich units [7]. Hydrogen sulphide is also commonly present in formation waters in regions of oil and gas production, naturally generated in situ from sulphate-bearing minerals through microbial sulphate reduction and (or) thermochemical sulphate reduction [8, 9]. As hydrogen sulphide is toxic at low concentrations and extremely corrosive to metal and cementitious materials, it poses risks to humans and can cause substantial damage in various industries [10–12], including engineered

barrier systems proposed for deep geological repositories for nuclear waste storage [13–16]. Due to the potential for the release of radionuclides following the corrosion of copper-coated steel containers in the presence of hydrogen sulphide [17], it is essential to understand the controlling factors that lead to the formation and distribution of elevated sulphide concentrations observed today and during glaciation events.

Microbially mediated reduction of sulphate by sulphate-reducing bacteria (SRB) is the main cause for the formation of H_2S in intracratonic sedimentary basins [18–20], where sulphate concentrations are often elevated in part due to the presence of sulphate minerals such as gypsum [6, 21] or anhydrite. Dissolved oxygen is commonly consumed at relatively shallow depths due to the presence of organic matter and reducing mineral phases [22–24], providing redox conditions suitable for sulphate reduction. The salinity of formation waters in sedimentary basins varies widely

ranging from fresh water near the surface to concentrated brines at depth [1, 2]. In these environments, salinity also varies over time, with subsequent impacts on the rate of sulphate reduction. Previous research provides evidence for the intrusion of glacial meltwater into permeable units of the Michigan Basin during the Pleistocene glaciation [25]. During deglaciation, increased hydraulic gradients, caused by accumulation of glacial meltwater below the melting ice sheet, led to infiltration of fresh water into the more permeable formations, significantly lowering fluid salinities and diluting water chemical compositions [25, 26]. Consequently, salinity was lowered at shallow and intermediate depths to such an extent that the activity of SRB was increased [18–20]. Although infiltration of meteoric water into shallow formations also occurs at present day, freshwater infiltration over geologic time is dominated by glacial meltwater infiltration [25, 27].

Reactive transport simulations have previously been conducted to investigate the impact of glaciation-deglaciation events on groundwater flow patterns, as well as geochemical and redox stability in sedimentary basins [23, 28, 29]. However, investigation of the effect of glaciation/deglaciation events on the generation and distribution of H_2S in these environments has only recently received attention [30]. Building on the work by Xie et al. [30], the main objective of this contribution is to evaluate the formation and attenuation of hydrogen sulphide during a glaciation event in a hypothetical sedimentary basin, partially constrained by observations from the Michigan Basin in southern Ontario. Through numerical modelling, we explore the interplay between physical and geochemical processes that affect the generation and persistence of hydrogen sulphide. We thereby contribute to an improved understanding of the processes governing the formation of sulphidic waters in relation to deep geological repositories hosted in low-permeability sedimentary rock environments. These simulations also increase our ability to assess the impact of possible future glaciation events on the geochemical evolution in sedimentary basins, which is of relevance in the safety assessment of long-term deep geological storage of used nuclear fuel. To achieve these objectives, the following tasks were undertaken:

(i) Develop a salinity-dependent sulphate reduction model constrained by observed and literature data, and implement the model into the parallelized reactive transport (RT) code MIN3P-THCm version 2.0 [31]

(ii) Conduct two-dimensional (2D) illustrative basin-scale RT simulations to investigate the formation of H_2S and its fate during a glaciation-deglaciation cycle

(iii) Provide a qualitative comparison of simulation results to observed data from the Michigan Basin

(iv) Conduct sensitivity analyses to investigate select factors controlling the formation and fate of H_2S, including the following: (1) $O_{2(aq)}$ concentration in glacial meltwater; (2) rate of biogenic sulphate reduction; (3) maximum thickness of the continental ice sheet in the region of interest

2. Field Observations from Southern Ontario

Groundwater with elevated H_2S concentrations is found at intermediate depths of sedimentary basins, including the Michigan Basin in southern Ontario, as depicted in Figure 1 [2, 32]. Also of note is that pore water in the deep subsurface is highly saline (brines), whereas fresh water exists in the shallow subsurface (Figure 1).

Carter et al. [2] presented the distribution of sulphidic groundwaters in southern Ontario based on groundwater chemistry data reported by companies drilling either shallow irrigation wells or deep petroleum wells up to 1,500 metres below ground surface (mbgs). Based on this data set, vertical distributions of sulphide, sulphate, iron, and chloride are presented in Figure 2. Samples with elevated sulphide concentrations ranging from 5.0×10^{-5} to 1.5×10^{-3} mol L^{-1} (1.6 to 48 mg L^{-1}) were collected at depths between 50 and 140 m. The highest sulphide concentrations approaching 2.0×10^{-3} mol L^{-1} (64 mg L^{-1}) were observed at a depth of around 100 m (Figure 2(a)). At greater depths (below 400 mbgs), sulphide concentrations were lower, ranging from 6.0×10^{-6} to 7.0×10^{-5} mol L^{-1} (0.2 to 2.2 mg L^{-1}). The data also show that higher sulphide concentrations were observed in samples with relatively low salinity (or Cl$^-$ concentration) [2] (Figure 2(b)). At depths exceeding 400 m, the concentration of Cl$^-$ is substantially higher, typically ranging between 4.0 and 9.0 mol L^{-1} (142 to 319 g L^{-1}). These observations are consistent with experimental findings in [33], which have shown that salinities greater than 130 g L^{-1} inhibit SRB *Desulphovibrio desulphuricans*. Above concentrations of 260 g L^{-1}, even the activity of extremely salt-tolerant SRB species is strongly inhibited [33–36]. In groundwater with lower salinity (< 40 g L^{-1}) and lower Cl$^-$ concentrations (< 1.0 mol L^{-1}, <35 g L^{-1}), observed sulphide concentrations vary substantially but often show elevated concentrations, ranging from 6.0×10^{-7} to 1.8×10^{-3} mol L^{-1} (0.02 to 58 mg L^{-1}) (see Figure A-2 in the Supplementary Information) [2].

Figure 2(a) shows that the concentration of sulphate is relatively uniformly distributed vertically, with concentrations near 2×10^{-3} mol L^{-1} (192 mg L^{-1}) at depths greater than 800 m. Sulphate concentrations span from 1.0×10^{-3} to 2.0×10^{-2} mol L^{-1} (96 to 1920 mg L^{-1}) at depths between 400 and 800 m and from 2.0×10^{-5} to 2.0×10^{-2} mol L^{-1} (2 to 1920 mg L^{-1}) at depths between 0 and 400 m (Figure 2). In general, sulphate is relatively common within these rock sequences, in part due to the presence of anhydrite, and thus available for biogenic sulphate reduction. Iron concentrations are low, ranging from 5.4×10^{-8} to 1.4×10^{-5} mol L^{-1} (3×10^{-3} to 0.8 mg L^{-1}) in the shallow subsurface up to 200 mbgs, but are higher in the deep subsurface, ranging from 5.4×10^{-7} to 3.1×10^{-3} mol L^{-1} (3×10^{-2} to 173 mg L^{-1}) (Figure 2(b)).

Isotopic results (i.e., $\delta^{18}O$ and δ^2H) for groundwater in the bedrock formations of southwestern Ontario indicate that shallow fresh water has a modern meteoric signature. In contrast, sulphidic waters at intermediate depths show an isotopic signature close to that of glacial meltwater, likely emplaced during retreat of the Laurentide Ice Sheet (LIS)
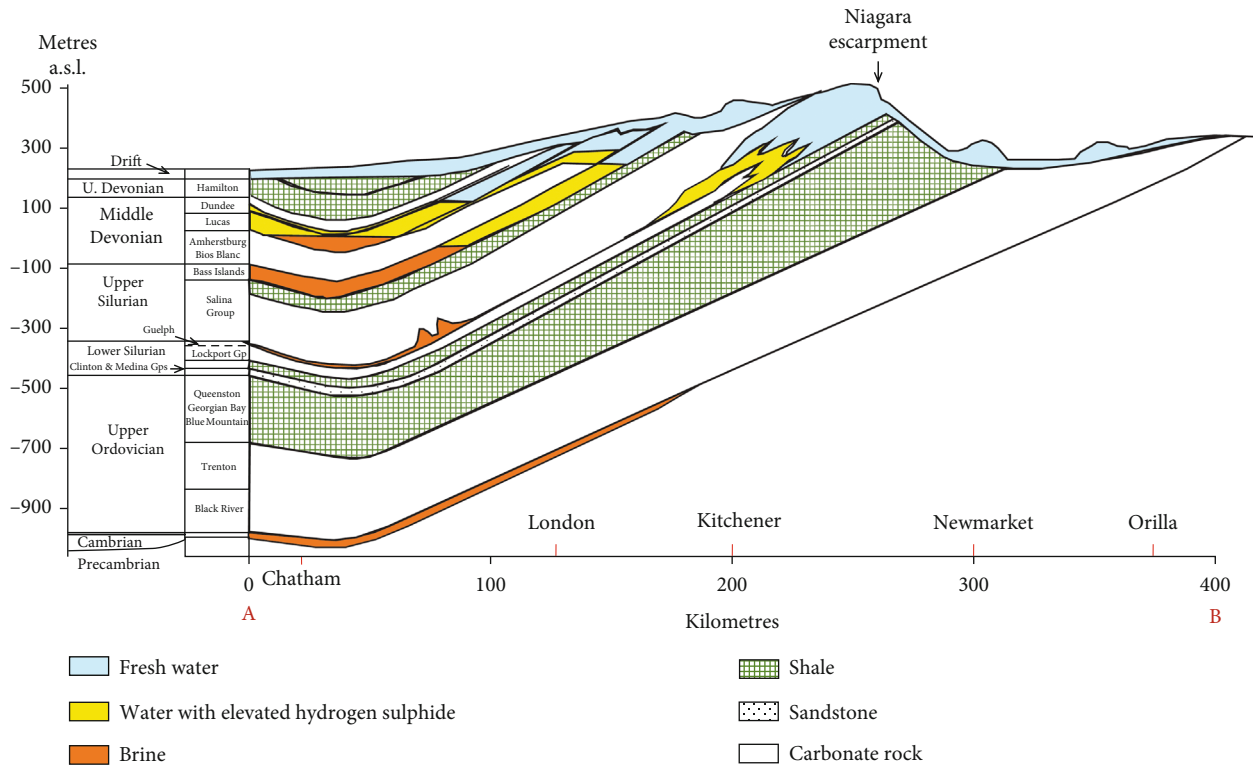
FIGURE 1: Conceptualized distribution of waters with elevated sulphide concentrations at the eastern flank of the Michigan Basin (modified from [32]). Sulphidic waters most commonly occur at intermediate depths of 100 to 400 metres below ground surface (mbgs). For the geographic location of the cross section A-B see Figure A-1 in the Supplementary Information.
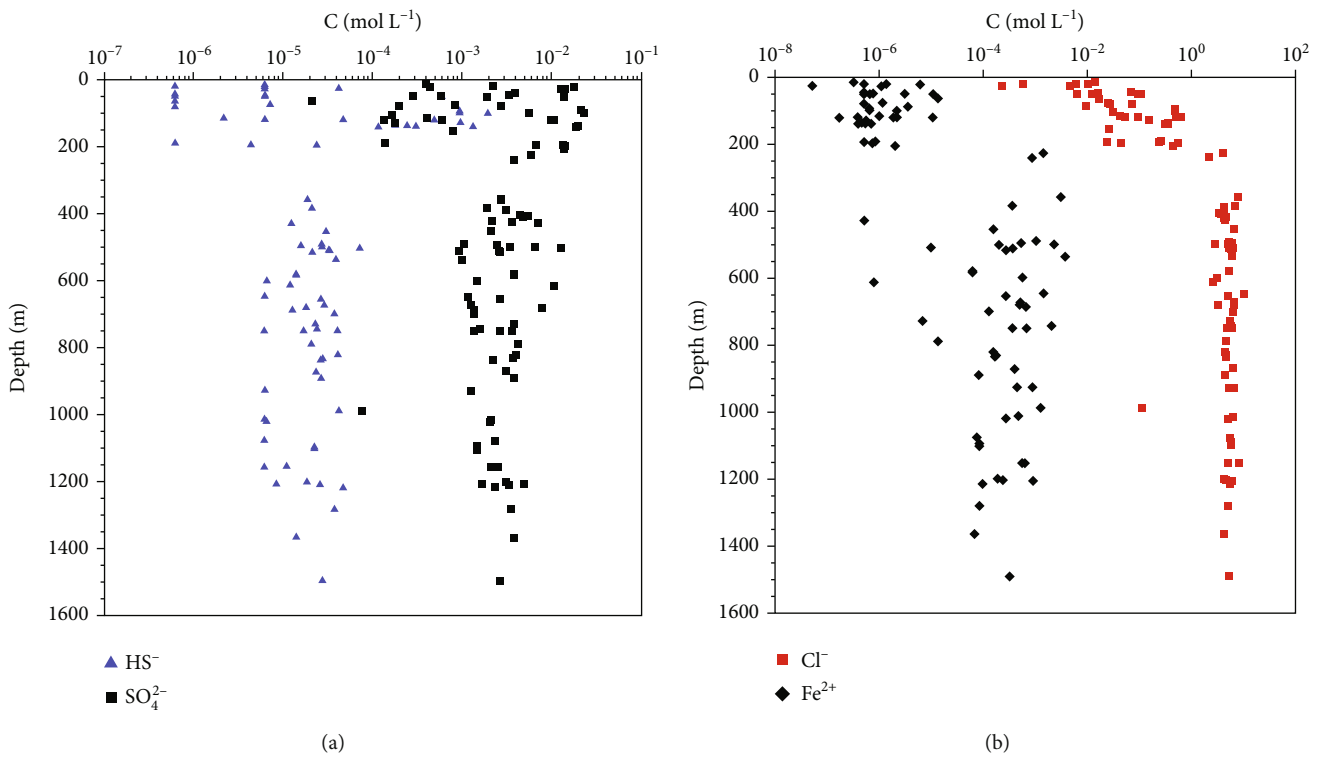

FIGURE 2: Observed sulphide (HS^-) and sulphate (SO_4^{2-}) (a) and chloride (Cl^-) and iron (Fe^{2+}) (b) concentrations (in mol L^{-1}) vs. sampling depth (based on data presented by Carter et al. [2]).
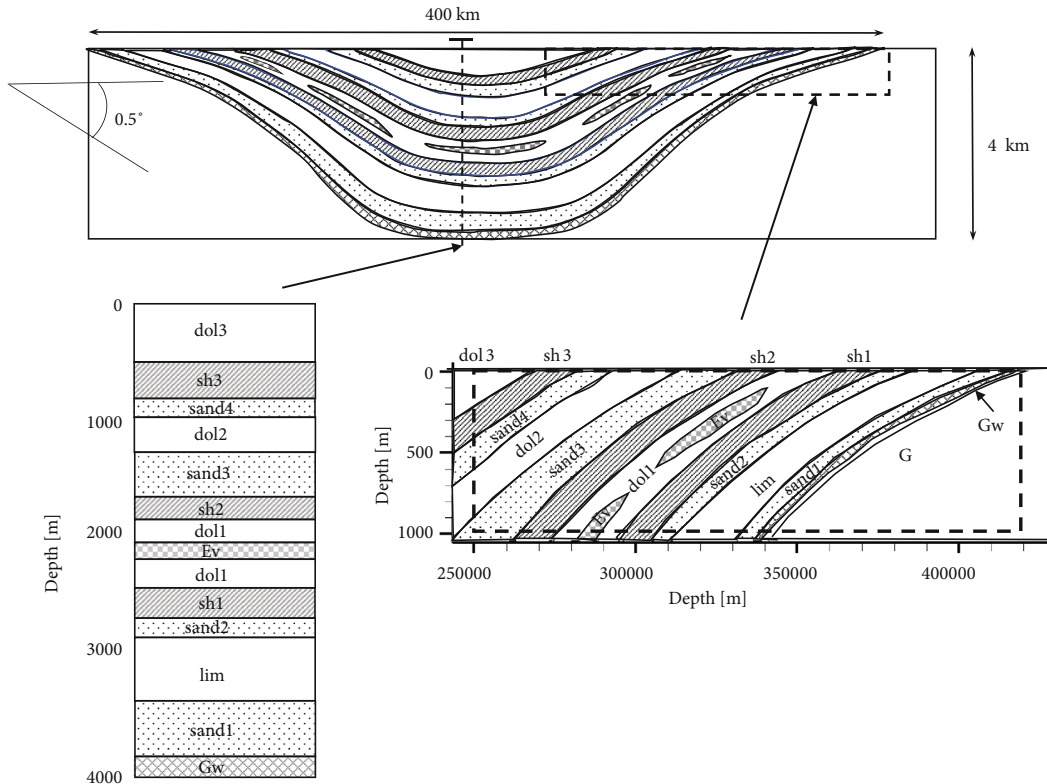
FIGURE 3: Geometry of hypothetical sedimentary basin and main hydrogeological units considered (modified based on Bea et al. [28]); subregion (dashed rectangular region on cross-section and enlarged subsection, excluding units Gw and G) for qualitative comparison with field observations from the Michigan Basin.

about 14,000 years ago [1, 32, 37–39]. These observations provide evidence for a more active shallow flow system during glaciation/deglaciation events.

3. Model Development and Parametrization

3.1. Modelling Approach. Simulations were performed for a hypothetical sedimentary basin considering the key features of several Palaeozoic sedimentary basins in North America, most notably the Michigan Basin, with simplifications to the topography, stratigraphic sequence, and material properties (Figure 3). The main physical and chemical processes considered were density-dependent flow, heat transport, diffusive-advective solute transport, and geochemical reactions (including hydrolysis, aqueous complexation, ion exchange, redox reactions, and mineral dissolution/precipitation). Porosity changes induced by one-dimensional mechanical stress, as a result of ice-sheet loading, and due to mineral dissolution-precipitation were also considered. In addition, permeability was updated based on the Carman-Kozeny model as a function of changing porosity (see [26, 27]). The simulations were initiated in an interglacial period and included a period of ice sheet advance and retreat over the sedimentary basin. The modelling approach builds on previous work by Bea et al. [23, 28, 29] and Xie et al. [30] but considers a more comprehensive geochemical reaction network.

For the current simulations, a 2D modelling framework was selected over a 3D or 1D approach. This choice was due to the following: (1) the intensive computational demand for RT simulations involving a complex geochemical network, making 3D basin-scale simulations computationally prohibitive; (2) the inability of a 1D model to capture the spatial variability and temporal evolution of flow, transport, and reaction processes in a sedimentary basin consisting of various sedimentary rock types and laterally varying surficial boundary conditions.

3.2. Simulation Domain and Discretization. The 2D simulation domain extends over a horizontal distance of 450 km and a vertical distance of 4 km (Figure 3). The hypothetical basin is composed of a sequence of interbedded layers of rocks including carbonates (dolostones dol1, dol2, dol3, and limestone lim), sandstones (sand1, sand2, sand3, and sand4), and shales (sh1, sh2, and sh3, as the main confining units). These units overlay a crystalline basement composed of granite (G); the upper 50 m of which is assumed to be weathered (Gw). Interbedded evaporites (Ev) are assumed to exist within the dolostone unit (Figure 3). The location of the data presented by Carter et al. [2, 3, 32] is generally consistent with the sedimentary rock sequence in a subregion of the simulation domain, extending from approximately 250 km to 420 km laterally and reaching a depth of 1 kilometre (see Figure 3). The 2D domain was discretized using 45,000 cells (i.e., 450 cells evenly distributed in the x < horizontal > direction and 100 cells in the z < vertical > direction).

3.3. Physical Parameters and Initial Conditions. The domain was assumed to be fully saturated, and the rocks in each unit were simulated as equivalent porous media. Physical and stratigraphic model parameters (i.e., porosity, hydraulic conductivity, elastic modulus, Poisson's ratio, volumetric heat capacity, material type, and thickness of units) are the same as described in previous studies (see Bea et al. [23, 28, 29], Xie et al. [30]). The main physical parameters (e.g., porosity, hydraulic conductivity, specific storage coefficient, and mechanical loading parameters) are material-specific and decrease with depth (see Table B-1, Figures B-1 to B-4 in the Supplementary Information, for more details, see Bea et al. [29]). Thermal parameters, including thermal conductivity and specific heat capacity, are also material-specific but do not change with depth within individual units (Figure B-5 in the Supplementary Information). The initial conditions for pressure head and total dissolved solids are also provided in the Supplementary Information (Figures B-6 and B-7).

3.4. Boundary Conditions for the Glaciation Scenario. The boundary conditions for flow, heat, and solute transport are based on Bea et al. [23] and Xie et al. [30] (see Figure B-8 in the Supplementary Information). For flow and solute transport, impervious boundary conditions are assumed for the two sides and the bottom of the domain. The same condition is applied for heat transport for the two sides, but a specified heat flux is assigned at the bottom to reproduce conditions in line with the geothermal gradient. Surface (i.e., top) boundary conditions for flow, solute transport, and heat transport are set either to represent ice-free conditions or conditions beneath a continental-scale ice sheet. The ice sheet is assumed to be cold-based during glacial advance (i.e., no recharge or discharge below the ice sheet) and warm-based during retreat (i.e., recharge or discharge permitted below the ice sheet). As discussed by Su et al. [40], previous studies have shown that the basal conditions beneath glaciers and ice sheets are frequently polythermal, with areas of both warm-based and cold-based conditions [41–44]. Most important to the current conceptual model is that meltwater generation during ice sheet advance is considered minor compared to the major meltwater generation expected during ice sheet retreat, in line with previous work by Provost et al. [45]. It is, therefore, reasonable to assume cold-based conditions during the period of glacial advance, with no recharge beneath the ice sheet, while ingress of meltwater into the domain occurs during retreat of the warm-based ice sheet. This approach is consistent with previous related RT modelling studies by Bea et al. [23, 29]. For further details, please refer to the Supplementary Information (Section B.2), Bea et al. [23], and Xie et al. [30].

3.5. Geochemical Reaction Network and Parametrization. The geochemical reaction network and corresponding thermodynamic parameters for the hypothetical sedimentary basin are based on Bea et al. [23, 29] and Xie et al. [30]. For the present study, the geochemical reaction network

was expanded to provide a detailed assessment of the formation and fate of sulphidic waters in the basin.

The main process associated with the formation of sulphidic waters in sedimentary rocks is considered to be the decomposition of organic matter linked to sulphate reduction. Two distinct pathways of sulphate reduction can be of importance in this context: biogenic sulphate reduction (BSR) and thermochemical sulphate reduction (TSR). For both pathways, the reactants are organic compounds and dissolved sulphate, and the products are H_2S and carbonate species [46], as represented in the following equation:

$$CH_2O_{(s)} + 0.5\,SO_4^{2-} \longrightarrow HCO_3^- + 0.5\,H_2S_{(aq)}. \quad (1)$$

BSR mainly occurs at lower temperatures (0-80°C) at shallow and intermediate depths. TSR is an alternative sulphate reduction pathway, dominant at temperatures exceeding 100°C in deep and hot reservoirs [5]. Such conditions are not relevant for our hypothetical 2D sedimentary basin simulations, since maximum temperatures remain well below 80°C.

Hypersaline porewater in the deep subsurface suppresses the activity of sulphate-reducing bacteria [33], while at intermediate depths, where the salinity is moderate and reduced conditions prevail, the activity of sulphate-reducing bacteria is expected to be high. This reaction is kinetically controlled and, in addition to being a function of salinity, depends on several factors including the abundance of reactive species (e.g., organic matter and sulphate) and inhibitors (e.g., dissolved oxygen, hydrogen sulphide, and ferric iron) [33, 36, 47–50]. The rate expression can be written as follows:

$$R_{SUL} = \varphi_{CH_2O_{(s)},l}\,k_{SUL}\,k_{sal}\left(\frac{[SO_4^{2-}]}{[SO_4^{2-}] + K_{SO_4^{2-}}}\right)\left(\frac{K_{O_{2(aq)}}}{[O_{2(aq)}] + K_{O_{2(aq)}}}\right)$$
$$\cdot \left(\frac{K_{HS^-}}{[HS^-] + K_{HS^-}}\right)\left(\frac{K_{Fe^{3+}}}{[Fe^{3+}] + K_{Fe^{3+}}}\right), \quad (2)$$

where $\varphi_{CH_2O_{(s)},l}$ is the volume fraction of organic matter in sedimentary rock unit l (dm³ $CH_2O_{(s)}$ dm⁻³ bulk), k_{SUL} is the rate coefficient for sulphate reduction by organic matter (mol dm⁻³ $CH_2O_{(s)}$ s⁻¹), k_{sal} is a salinity inhibition factor (-), and K_i (mol L⁻¹ H_2O) is the relevant half saturation or inhibition constants for sulphate, O_2, hydrogen sulphide, and ferric iron. Because a linear correlation between salinity and chloride concentrations has been observed in groundwater in south-eastern Ontario (see Figure A-2 in the Supplementary Information), the salinity inhibition term is here expressed as a function of chloride concentration.

$$k_{sal} = \begin{cases} 1 & , \text{if } [Cl^-] < C_L, \\ \dfrac{[\cos(a*[Cl^-]+b)+1]}{2} & , \text{if } C_L \le [Cl^-] \le C_H, \\ 0 & , \text{if } [Cl^-] > C_H, \end{cases}$$
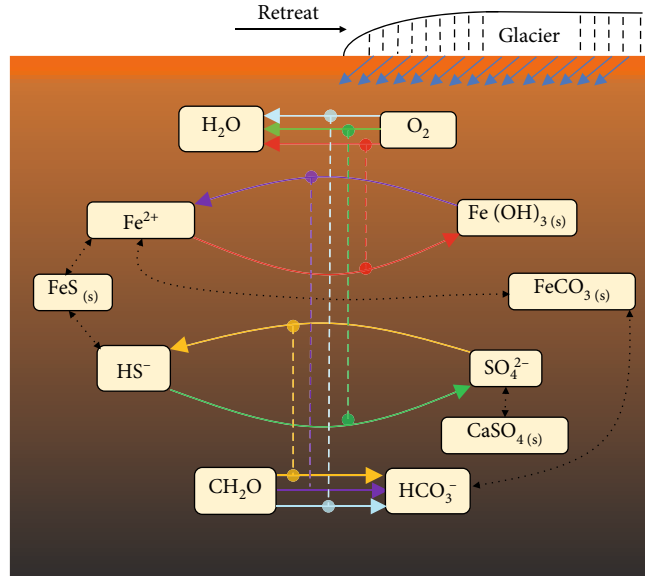$$(3)$$

FIGURE 4: Simplified biogeochemical reaction network related to the formation and fate of sulphidic waters in sedimentary rocks.

where $[Cl^-]$ is the concentration of chloride (mol L^{-1}). The coefficients a and b can be determined based on C_H and C_L, where C_L is the chloride concentration below which there is no inhibition of sulphate reduction, and C_H is the chloride concentration above which sulphate reduction is completely inhibited. Using this formulation, the salinity inhibition factor ranges from 0 to 1. The rate of biogenic sulphate reduction between C_H and C_L is assumed to follow a cosine function, with the parameters a and b defined according to equations (4) and (5), respectively.

$$a = \frac{180}{C_H - C_L}, \tag{4}$$

$$b = -aC_L. \tag{5}$$

The values of C_H and C_L used for the current simulations were 1.41 mol L^{-1} and 0.076 mol L^{-1}, respectively, which were calibrated based on the observational data in Figure 2. Parametrization of the rate expression for sulphate reduction (equation (2)) is provided in the Supplementary Information (Section B.3).

Hydrogen sulphide produced by sulphate reduction undergoes hydrolysis, and in the presence of ferrous iron, it tends to precipitate as sparingly soluble metal sulphides (Figure 4).

$$HS^- + Fe^{2+} \rightleftharpoons FeS + H^+. \tag{6}$$
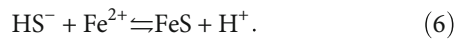
If reducing conditions cannot be maintained, for example, due to the ingress of dissolved oxygen, dissolved sulphide can also be reoxidized.

$$HS^- + 2 O_{2(aq)} \longrightarrow SO_4^{2-} + H^+. \tag{7}$$
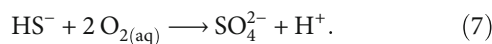
Under these conditions, ferrous iron also tends to become oxidized, leading to the production of relatively insoluble Fe^{3+}. In addition, the dissolution and precipitation of sulphate minerals (e.g., anhydrite) can act as a source or sink for SO$_4^{2-}$ (Figure 4).

$$CaSO_4 \rightleftharpoons SO_4^{2-} + Ca^{2+}. \tag{8}$$
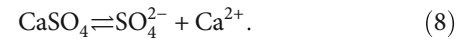
To simulate the above reactions the geochemical reaction network includes 13 geochemical components (i.e., Ca^{2+}, Na$^+$, Mg^{2+}, K$^+$, Cl$^-$, SO$_4^{2-}$, H$^+$, CO$_3^{2-}$, HS$^-$, O$_{2(aq)}$, Fe^{2+}, Fe^{3+}, and dissolved organic carbon represented by CH$_2$O), 47 aqueous complexes, three intra-aqueous kinetic reactions including the oxidation of dissolved sulphide, ferrous iron and organic carbon by oxygen, and nine minerals (i.e., calcite, anhydrite, halite, dolomite, ferrihydrite, iron sulphide (e.g., FeS), siderite, chlorite, and biotite), as well as ion exchange reactions. The component HS$^-$ represents total dissolved sulphide, including H$_2$S. Similarly, the total concentrations of Fe^{2+} and Fe^{3+} include hydrolyzed and complexed species. Minerals were chosen based on their abundance in sedimentary rocks in the Michigan Basin and other basins [1, 23, 51] and in underlying crystalline basement rocks. In addition, minerals providing important solubility controls for Fe^{2+}, Fe^{3+}, and HS$^-$ were also considered. The complete geochemical reaction network and all relevant thermodynamic and kinetic parameters for the simulations are provided in Section B.3 in the Supplementary Information (Table B-2 to B-6 in Supplementary Information).

In the current model, temperature effects on biogenic sulphate reduction are not considered. This simplification has no significant impact on the simulated sulphide distribution. This is because simulated temperatures at intermediate depth, where higher hydrogen sulphide concentrations are observed, do not vary significantly over the course of the simulation (Figures C-1 and C-2 in the Supplementary Information). However, all equilibrium constants were updated using the van't Hoff equation based on the spatial

TABLE 1: Description and key parameter values for the simulations.

Case	Description	$[O_{2(aq)}]^{(a)}$ (atm)	k_{SUL} (mol dm^{-3} CH$_2$O$_{(s)}$ s^{-1})	Hmax$^{(b)}$ (m)
BASE	Reference case	0.21	8.5×10^{-12}	2,000
S1	Increase of $O_{2(aq)}$ concentration in glacial meltwater at the top boundary	1.00	8.5×10^{-12}	2,000
S2	Increase of sulphate reduction reaction rate by one order of magnitude	0.21	8.5×10^{-11}	2,000
S3	Maximum ice sheet thickness 3,000 m	0.21	8.5×10^{-12}	3,000

(a): partial pressure of $O_{2(aq)}$ in meltwater; (b): Hmax–maximum ice sheet thickness in the region of interest.

and temporal distribution of temperature and enthalpy change values provided in the model database.

The initial water compositions in the different geological units and boundary conditions for the interglaciation scenario are identical to Bea et al. [23] except for the additional components HS$^-$, Fe^{2+}, and Fe^{3+}, which were assigned in the same way as in Bea et al. [23] and Xie et al. [30]. Concentrations in Table B-8 in the Supplementary Information were directly assigned to the corresponding units for depths greater than 500 mbgs. Concentrations were linearly interpolated with those of meteoric water between the ground surface and a depth of 500 mbgs and then equilibrated with the local minerals (Table B-2 and B-7 in Supplementary Information), if present in the respective formation (Table B-6 in Supplementary Information). Sulphide concentrations in porewater in the deep subsurface are fairly low and were assumed to be in equilibrium with iron sulphide minerals. The formation water in units G, Gw, sand1, and sand2 is hypersaline with high fluid density at depths greater than 500 mbgs, while the meteoric water is rich in $O_{2(aq)}$ with low fluid density.

3.6. Simulation Cases. To evaluate the impact of select model parameters, three sensitivity cases (i.e., S1 to S3 in Table 1) were considered in addition to the reference case (described above, BASE in Table 1). The sensitivity cases were as follows: scenario 1 (S1): elevated $O_{2(aq)}$ concentration in infiltrating glacial meltwater; scenario 2 (S2): increased rate of biogenic sulphate reduction; and scenario 3 (S3): increase of the maximum ice sheet thickness (Hmax) (i.e., 1,000 m higher than the reference case).

4. Results and Discussion

For the reference case (BASE), the evolution of flow, density, and thermal conditions, as well as major ion chemistry (excluding sulphide and iron species) during interglaciation and glaciation-deglaciation periods are reported in detail by Bea et al. [23, 29]. Figure C-1 in the Supplementary Information summarizes the flow, solution density, and temperature results at the end of the interglaciation simulation. These results serve as the initial conditions for the glaciation-deglaciation simulations for the reference case (BASE) and the sensitivity cases. In the following, we present and discuss simulation results emphasising those results associated with the evolution of sulphidic waters in

the sedimentary rock units. We also introduce key aspects of the system evolution to provide the necessary context.

4.1. Reference Case (BASE)

4.1.1. Flow, Density, and Thermal Evolution. Simulation results for flow, density, and temperature during the glaciation-deglaciation cycle show that the active flow regime generally remains restricted to shallow depths (less than 300–400 mbgs). This is due to the presence of dense brines at depth and the near horizontal layering of the hydrogeological units that form the basin (Figure 5; Figures C-2 to C-3 in the Supplementary Information, note the significant exaggeration; for details, see [23, 29]).

The main driving force for flow differs between the periods of ice sheet advance (stage I) and retreat (stage III). With the advancement of the continental glacier (up to 2,000 m in thickness), point pressure heads in the deformable units increase due to ice sheet loading (e.g., stage I while ice is accumulating, T = 10,000 years, and during the glacial maximum, T = 17,000 years, stage II) throughout the basin (Figure C-3). During retreat of the ice sheet, pressure heads increase beneath the ice sheet in shallow permeable units (Figure C-3, T = 20,000 years) due to the hydraulic connection between the warm-based melting ice sheet and the sedimentary units. During this period, dilute meltwater with elevated dissolved oxygen enters the aquifers beneath the melting ice sheet, resulting in pockets of low-salinity water and also leading to displacement of pore waters at greater depths (Figure 5).

The distribution of fluid salinity changes with the advance/retreat of the ice sheet depending on the depth of meltwater penetration and mixing with resident pore water (Figure 5). During glacial advance (stage I), the change of fluid salinity is small (see also Figure C-4 in the Supplementary Information). However, significant increases (up to 200 g L^{-1}) and decreases (up to -160 g L^{-1}) of the fluid salinity occur during glacial retreat (stage III, T = 20,000 years). This evolution can be seen along the layers with higher hydraulic conductivities (i.e., sandstones and dolostone dol2) towards the right- and left-hand sides of the domain, respectively. This results in enlarged regions of lower fluid density within the sand3, dol2, and sand4 units on the right-hand side of the basin cross-section (Figure 5 and Figure C-4 in the Supplementary Information). This evolution of salinity coincides with the retreat of the ice sheet, resulting in high hydraulic heads above the right-hand side of the domain. High heads push meltwater downwards
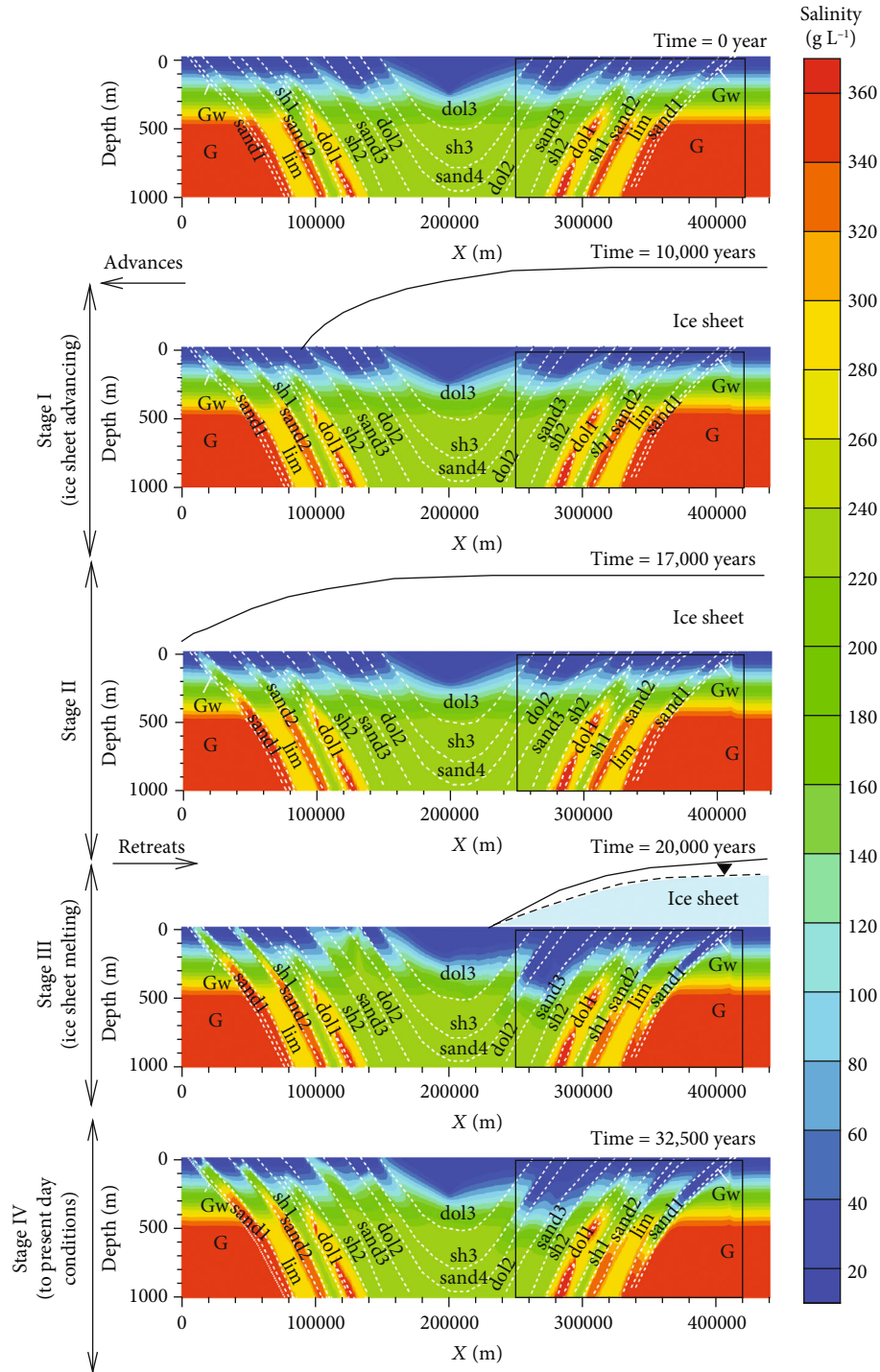
FIGURE 5: Simulated spatial distributions of fluid salinity for the reference case (BASE) during the glaciation-deglaciation cycle (i.e., at 0, 10,000, 17,000, 20,000, and 32,500 years). The black rectangle in the contour plots indicates the data extraction region for comparison with field observations from the sedimentary rock units (i.e., horizontal from 250 to 420 km and vertical from 0 to 1000 mbgs).

and into the rock layers. At 32,500 years (stage IV), 10,000 years after the complete retreat of the glacier, the salinity change relative to initial conditions (Figure C-4) indicates progressive recovery towards the initial condition (Figure 5).

4.1.2. Effect of Glaciation Cycle on Distribution of Waters with Elevated Sulphide. The following discussion of the

results focuses on the portion of the domain, which is delineated by the rectangular subregion in Figures 5–7, used for comparison with observational data from the Michigan Basin. The reference case (BASE) BSR rates and the variation of the rates during a glaciation-deglaciation cycle are shown in Figure 6. During quasisteady state interglacial conditions (e.g., T = 0 years), the sulphate reduction rates (R_{SUL})
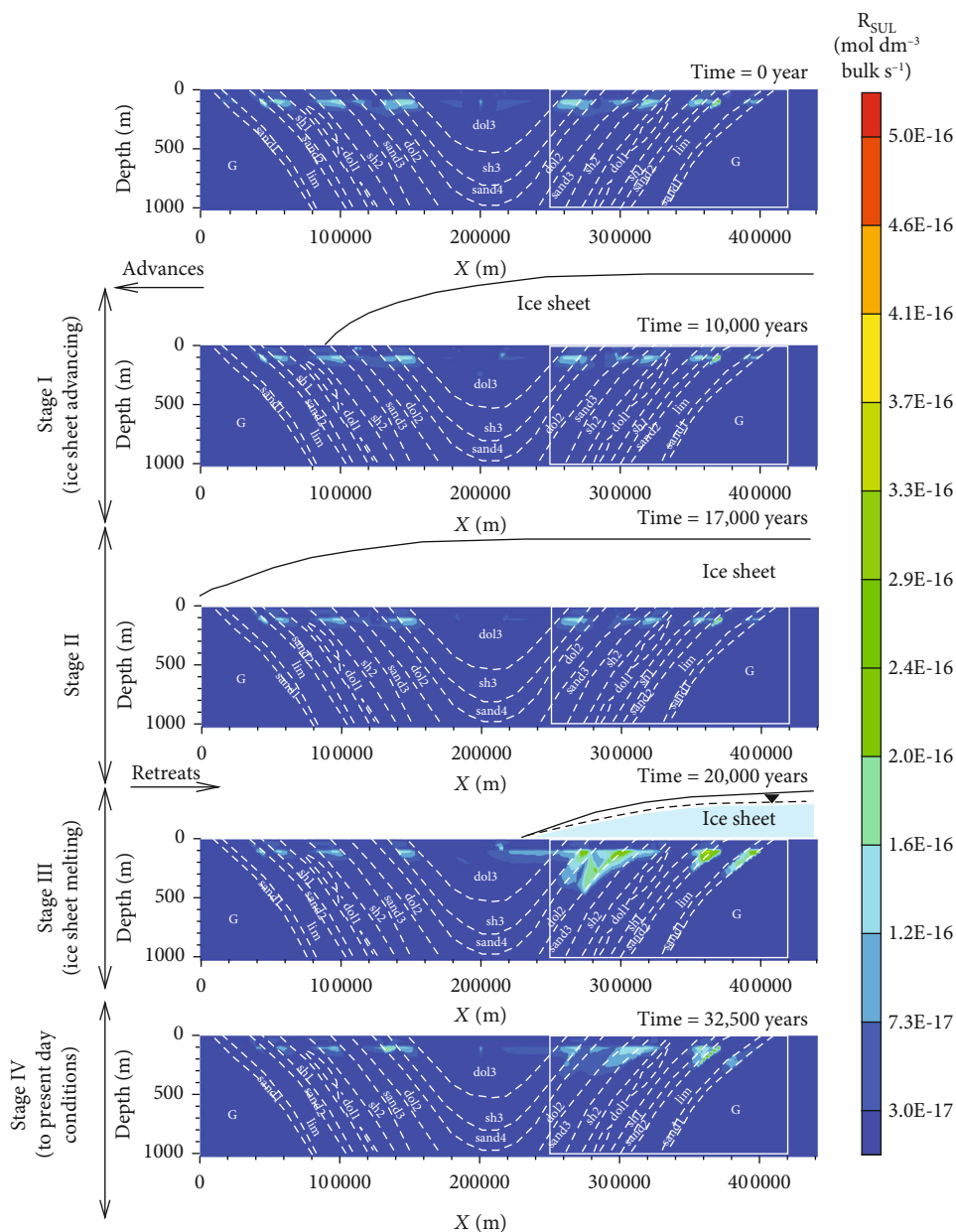
FIGURE 6: Simulated spatial distributions of the biogenic sulphate reduction rate (R_{SUL}) by SRB for the reference case (BASE) during the glaciation-deglaciation cycle (i.e., at 0, 10,000, 17,000, 20,000, and 32,500 years). The white rectangle in the contour plots indicates the data extraction region for comparison with field observations from the sedimentary rock units.

are highest at depths between 70 and 160 mbgs throughout most of the domain (Figure 6, T = 0.0 years). This depth interval corresponds to depths transitioning from low to high salinity (Figure 5, T = 0.0 years).

Sulphate reduction rates are higher in shales than in sandstones, dolostone, or limestone. This is due to lower $O_{2(aq)}$ concentrations in shales caused by their extremely low hydraulic conductivities and a relatively higher abundance of solid organic matter (Table B-6 in the Supplementary Information). These results are consistent with experimental data on SRB activities in oil shales reported in [19, 20].

During interglacial conditions (T = 0 years), elevated concentrations of HS$^-$ (total dissolved sulphide) extend up

to 200 mbgs in dolostones dol2 and dol3 (Figure 7) due to a lack of Fe-bearing mineral phases in these units (Supplementary Information, Table B-6). During stages I and II (advance and glacial maximum), the top boundary is closed due to the assumed cold-based conditions underneath the ice sheet, thus preventing recharge and $O_{2(aq)}$ intrusion [23]. Both R_{SUL} (Figure 6, T = 10,000 and 17,000 years) and HS$^-$ concentrations (Figure 7, T = 10,000 and 17,000 years) remain relatively unchanged in comparison to interglacial conditions (Figure 8), with one exception. The simulation predicts that $O_{2(aq)}$ concentrations decline at shallow depth (25 mbgs) in unit dol2, accompanied by an increase in HS$^-$ concentrations
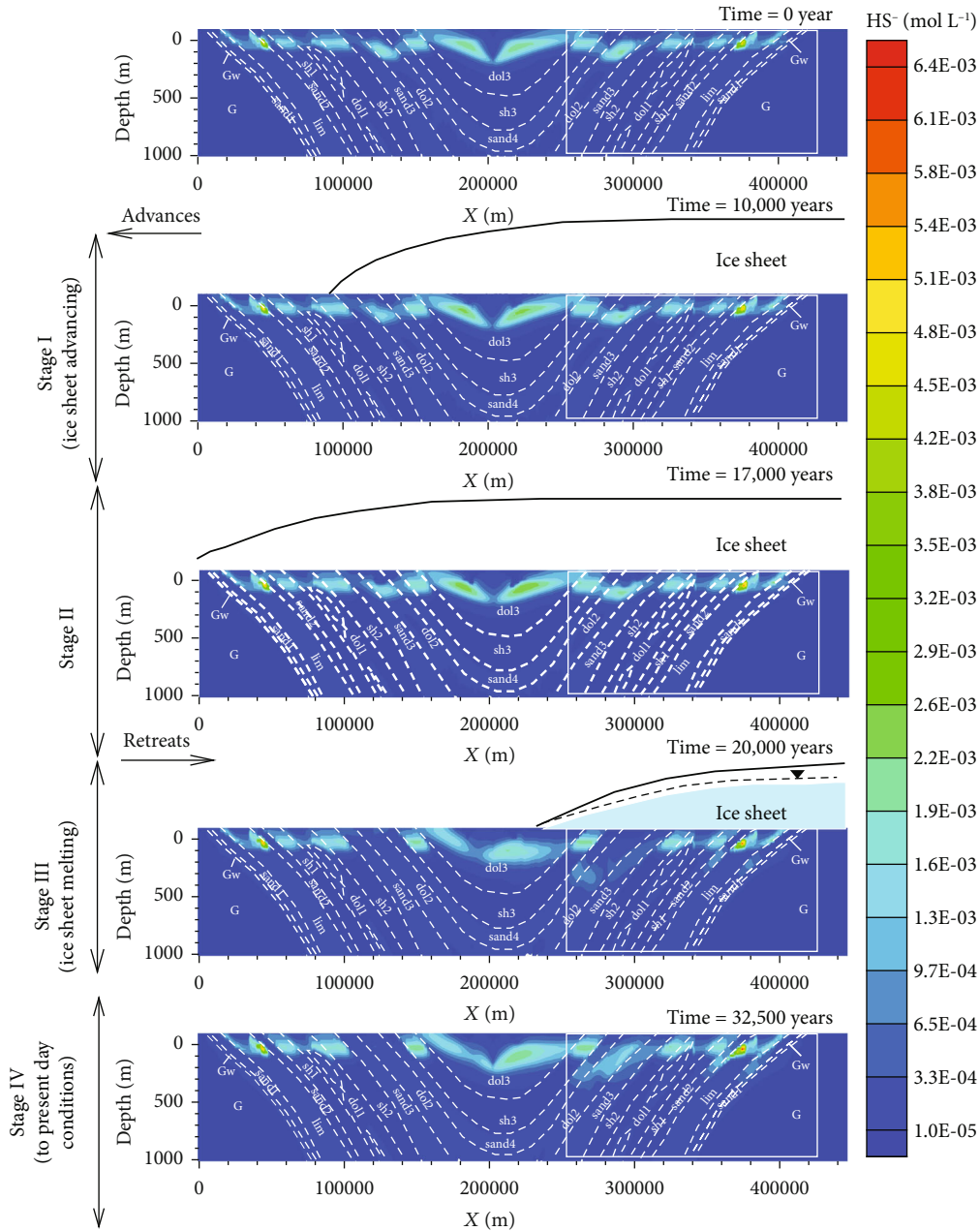
FIGURE 7: Simulated spatial distributions of HS⁻ (total dissolved sulphide) concentrations for the reference case (BASE) during the glaciation-deglaciation cycle (i.e., at 0, 10,000, 17,000, 20,000, and 32,500 years). The white rectangle in the contour plots indicates the data extraction region for comparison with field observations for sedimentary rock units.

(Figure 8(c)). The results for unit dol2 can be explained by a relatively high hydraulic conductivity, accompanied by low porosity values in this dolostone, leading to a strong hydraulic and geochemical response in layers with higher hydraulic conductivity once recharge is cut off. Conditions in the shales remain unchanged as a result of hydraulic isolation (results not shown). Overall, the simulations suggest that during the period of glacial advance and in the presence of cold-based conditions, geochemical conditions remain relatively stable throughout the basin. Changes in salinity and HS⁻ concentrations remain small during this phase (Figures C-4 and C-5 in the Supplementary Information).

At the end of stage II (T = 17,000 years), the top boundary transitions from cold- to warm-based, and hydraulic heads at the ground surface boundary are assumed to be 90% of the thickness of the melting ice sheet. During stage III, an asymmetric and nonstationary hydraulic head distribution is assigned to the top boundary as the ice sheet progressively retreats. This dynamic hydraulic boundary condition has a larger impact in the rock units with higher hydraulic conductivities (Figures 5 and 7 at 20,000 years, Figure 8: sandstones, and dolostones dol2 and dol3, see also Figures C-4 and C-5 in the Supplementary Information).
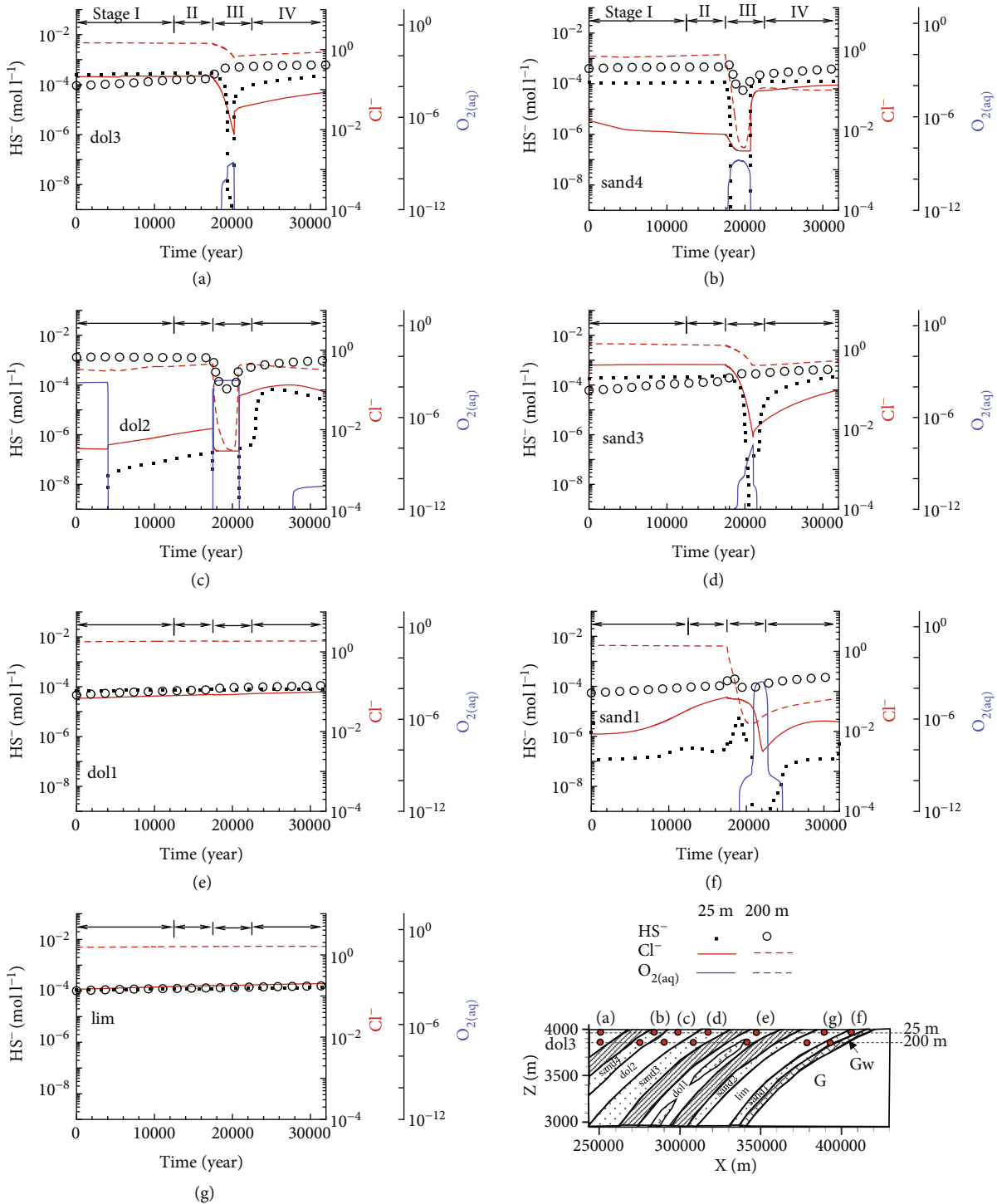
FIGURE 8: Simulated temporal evolution of Cl^-, HS^-, and dissolved $O_{2(aq)}$ concentrations at 25 and 200 mbgs for the reference case (BASE). (a)–(g) Observation points in units dol3, sand4, dol2, sand3, dol1, sand1, and lim, respectively. If the profiles for $O_{2(aq)}$ are not visible for a specific depth and unit, simulated $O_{2(aq)}$ concentrations remain below 1.0×10^{-12} mol L^{-1}.

Consequently, salinities and HS^- concentration changes are larger in the higher hydraulic conductivity units (Figures 5 and 7, Figures C-4 and C-5 in the Supplementary Information). During the retreat of the ice sheet, the concentrations of Cl^- (as a surrogate for salinity) and HS^- decrease at a depth of 25 mbgs, whilst those of $O_{2(aq)}$ increase at the observation points in the units dol3, sand3,

and sand4 (Figures 8(a), 8(b), and 8(d)). These results indicate that the ingress of oxygenated fresh water leads either to the displacement of water containing HS^- or to the oxidation of resident HS^-. The change in Cl^- concentrations has no significant effect on HS^- concentrations at this depth. Similar results can be observed in units dol2 and sand1 (Figures 8(c) and 8(f)); however, in these units, HS^-

concentrations at 25 mbgs are already very low prior to the onset of deglaciation. Notably, no significant impact of deglaciation is seen in units dol1 and lim (Figures 8(e) and 8(g)), due to the low hydraulic conductivity of these units (Figure B-2, Supplementary Information).

The response at a depth of 200 mbgs is delayed and also characteristically different. In units dol3 and sand3, HS$^-$ concentrations increase accompanied by a decrease in Cl$^-$ concentrations (salinity), while redox conditions remain reducing (Figures 8(a) and 8(d)). These results indicate that the decline in salinity leads to increased sulphate reduction rates (visible in Figure 6), causing sulphide concentrations at this depth to rise (see also Figure 7 and Figure C-5 in the Supplementary Information). In addition, ingress of water with higher sulphide concentrations from above (Figure 7) may also contribute to the increase in sulphide concentrations at this depth during the period of deglaciation. Initially, similar behaviour can be observed in sand1 (Figure 8(f)) and to a lesser degree in sand4 (Figure 8(b)). However, subsequently, HS$^-$ concentrations decrease, indicating the displacement of resident pore water by ingressing fresh water with lower sulphide concentrations from above. Although HS$^-$ concentrations decline, an increase in O$_{2(aq)}$ is not observed at 200 mbgs, suggesting that O$_{2(aq)}$ is consumed closer to the ground surface. This is due to the oxidation of dissolved organic matter (DOM) and HS$^-$, as well as the oxidative dissolution of Fe-bearing silicates. Similar to the observation point at 25 mbgs, dol2 responds most rapidly at 200 mbgs, and a decrease in Cl$^-$ concentrations is immediately accompanied by a decline in HS$^-$ concentrations (Figure 8(c)). This indicates that HS$^-$ concentrations are dominated by displacement with pore water from above and not a change in sulphate reduction rates as a function of salinity changes. O$_{2(aq)}$ concentrations remain below the lower cut-off limit, despite the rapid hydraulic response of this unit (Figure 8(c)). As at shallower depth, no significant changes are seen in units dol1 and lim, due to their low hydraulic conductivities.

Overall, these results indicate that the presence of O$_{2(aq)}$ in the infiltrating meltwater decreases sulphate reduction rates, while a decline in salinity increases the reaction rates. These two competing processes, together with displacement of resident pore water, lead either to an increase or decrease in sulphide concentrations. The simulations also indicate that, for the subregion of interest, deglaciation leads to a decrease of sulphide concentrations at shallow depth and an increase at greater depth. In the most permeable units (sand3, sand4, and dol2), this effect is seen in the simulations up to a depth of approximately 500 mbgs, while no effect on HS$^-$ concentrations is seen in the less permeable units (dol1 and lim), even at very shallow depths of 25 mbgs (Figures 7 and 8, Figure C-5 in the Supplementary Information).

After disappearance of the ice sheet, the top boundary reverts to interglacial conditions, and the perturbed flow field begins to recover, slowly approaching the initial conditions (Figure C-3). O$_{2(aq)}$ concentrations decrease, while salinity and the concentrations of Cl$^-$ and HS$^-$ approach values present prior to the onset of the glaciation cycle (Figures 5–8). At 32,500 years, the sulphate reduction rates

decline in the area of interest and approach rates prior to the glaciation-deglaciation cycle (Figure 6, T = 32,500 years). The simulations do not fully recover to the initial condition, due to the relatively short duration of the interglacial period following the disappearance of the ice sheet. It is likely that a simulation covering only a single glaciation-deglaciation cycle may not fully capture the long-term hydraulic and geochemical response that would be associated with multiple glaciations.

4.1.3. Comparison to Field Data. Due to the simplified representation of the simulated sedimentary basin and the hypothetical glaciation-deglaciation scenario, direct comparison of the results to the observed data collected in southern Ontario [2, 3, 32] (Figure 2) is not possible. However, a qualitative comparison is still valuable for assessing and interpreting the simulation results. In Figure 9, the simulated results at 32,500 years, representing interglacial conditions, are compared to present-day field observations compiled by Carter et al. [2]. To facilitate the comparison, we have extracted the simulated data from the subregion of interest (see Figure 3).

All simulated data from the crystalline basement (units G and Gw) were excluded from this comparison because field data were only collected from sedimentary rock units. Simulated results are shown in light grey symbols, with solid lines showing the mean concentrations of all simulated data points from specific depths. Observed concentrations are depicted as black triangles. Due to the lack of observed dissolved oxygen concentrations, only simulated data of O$_{2(aq)}$ are shown (Figure 9(b)). Below 100 mbgs, simulated O$_{2(aq)}$ concentrations are below 10^{-12} mol L^{-1} (corresponding to 3.2 × 10^{-5} mg L^{-1}).

Overall, the simulated results are in good agreement with observed data for HS$^-$, SO$_4$$^{2-}$, Cl$^-$, Fe^{2+}, and Mg^{2+} (Figure 9). Wide scattering of concentrations at specific depths can be seen for most components, which is expected considering that data at each depth stem from multiple sedimentary rock units. Except for Fe^{2+}, the scattering is mainly limited to a depth of approximately 300 m for simulated data and 200 m for observed data; these are the depth intervals most significantly affected by the glaciation-deglaciation cycle.

It is important to note that not many observations are available between 200 and 400 mbgs because the data either originates from water supply projects (< 200 mbgs) or from the oil and gas industry focusing on the deeper subsurface (> 400 mbgs)) [2]. Nevertheless, the simulation results and observed data are consistent with data from McIntosh and Walter [27], showing that fresh water significantly diluted saline brines in the upper Antrim Shale across the northern margin of the Michigan Basin, as evidenced by a decrease (up to 80%) in bromide concentrations to a depth of 300 m.

The maximum concentrations of HS$^-$ for simulated (4.7 × 10^{-3} mol L^{-1} or 155 mg L^{-1}) and observed data (1.9 × 10^{-3} mol L^{-1} or 63 mg L^{-1}) are located at almost the same depth (i.e., around 100 mbgs, Figure 9(a)). The maximum average simulated concentration of 1.1 × 10^{-3} mol L^{-1} (36 mg L^{-1}) was predicted at the same depth. Simulated HS$^-$ concentrations in the shallow subsurface show a wide range of concentrations due to the local presence of O$_{2(aq)}$,

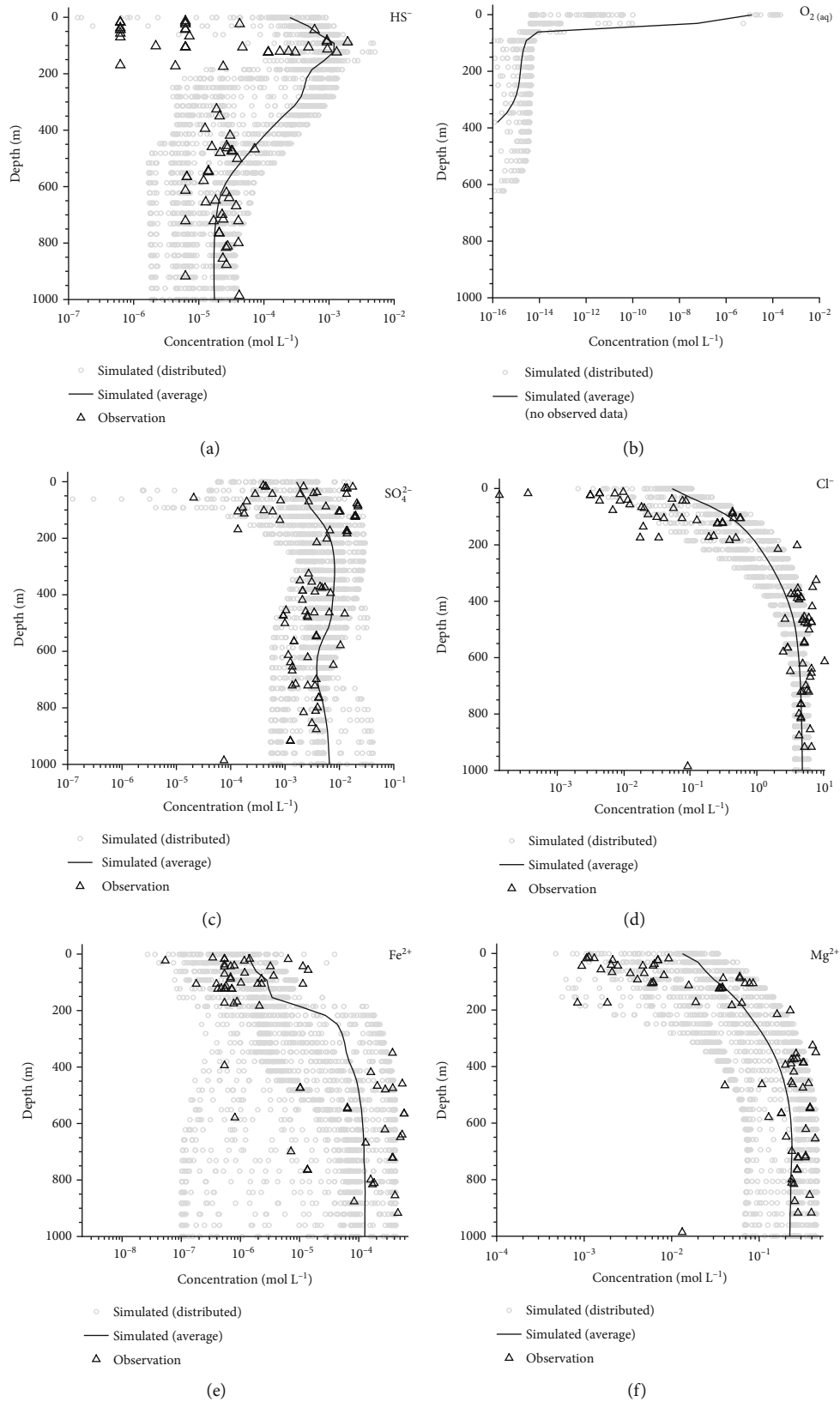FIGURE 9: Comparison of observed and simulated concentrations of HS^- (a), $O_{2(aq)}$ (b), SO_4^{2-} (c), Cl^- (d), Fe^{2+} (e), and Mg^{2+} (f) for the reference case (BASE). Simulated data were extracted from the subregion depicted in Figure 3, excluding data points in the crystalline basement rocks (G and Gw). The circles in light grey represent simulated concentrations, while the solid lines depict depth-specific mean values of the simulated data. Observed data shown as triangles are from Carter et al. [2].
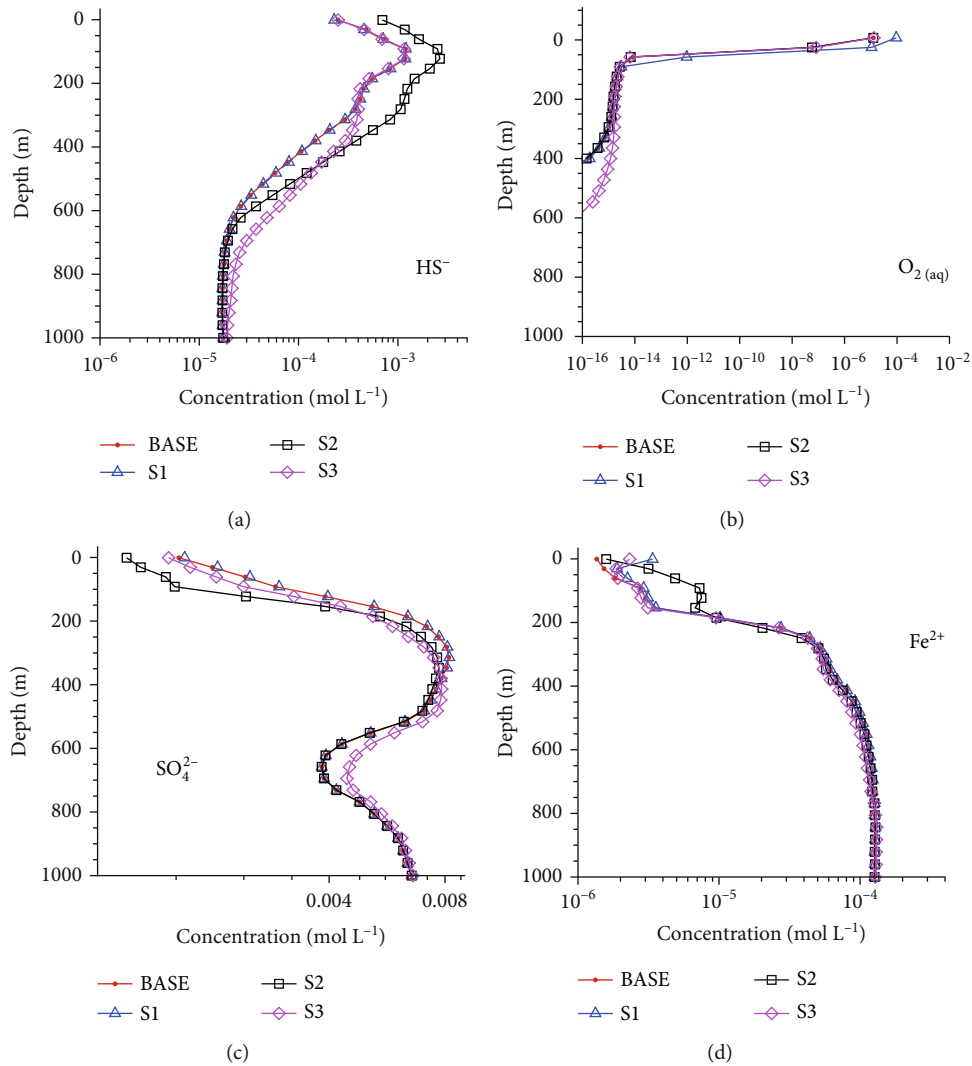
FIGURE 10: Comparison of the mean of simulated concentrations of HS$^-$ (a), O$_{2(aq)}$ (b), SO$_4{}^{2-}$ (c), and Fe^{2+} (d) at different depths for the reference case (BASE) with sensitivity cases S1, S2, and S3. Simulated concentrations were extracted from the subregion depicted in Figure 3, excluding data points in the crystalline basement rocks (G and Gw).

consistent with observations. Larger variability in HS$^-$ concentrations is seen in the depth interval between 100 and 200 mbgs in the observed data, relative to the simulated data, possibly suggesting a local lack of sulphate or the presence of O$_{2(aq)}$ in groundwater, not captured by the model. In the deeper subsurface (below a depth of 450 m), simulated HS$^-$ concentrations are lower, in the range of 2.0×10^{-6} to 4.0×10^{-5} mol L^{-1} (6.6×10^{-2} mg L^{-1} to 1.3 mg L^{-1}) with an averaged value of 1.5×10^{-5} mol L^{-1} (0.5 mg L^{-1}), showing very good agreement with the observed data.

Although observational data are not available between 200 and 400 mbgs, the simulation results indicate that elevated HS$^-$ concentrations gradually decline to concentrations present in the deeper subsurface and are inversely correlated with salinity, as implied by the Cl$^-$ concentration variation with depth (Figure 9(b)). This is consistent with the fact that hypersaline conditions in the deep subsurface suppress the activity of sulphate-reducing bacteria [52]. Simulated and observed Fe^{2+} concentrations are lower in the shal-

low subsurface (< 200 mbgs) than at greater depths (Figure 9(e)). This is at least in part due to the oxidation of Fe^{2+} by O$_{2(aq)}$ close to the top boundary and precipitation of FeS owing to higher HS$^-$ concentrations in this depth interval. Mg^{2+} concentrations are also in good agreement with the observed data and follow a similar trend to Cl$^-$ (Figure 9(f)).

4.2. Sensitivity Analysis Results. A comparison of the sensitivity analysis results to the results of the reference case (BASE) is provided in Figure 10 for HS$^-$, O$_{2(aq)}$, SO$_4{}^{2-}$, and Fe^{2+}. In addition, the sensitivity analysis results are compared to field observations in the Supplementary Information (Figures C-6 – C-8).

The results demonstrate that an increase of O$_{2(aq)}$ concentrations in the infiltrating meltwater has a very limited effect on the overall results relative to the reference case (Figure 10, Figure C-6), with essentially no differences seen in the HS$^-$ and SO$_4{}^{2-}$ concentration profiles. These results suggest that, although O$_{2(aq)}$ concentrations were increased

TABLE 2: Comparison of maximum and minimum component concentrations within the region of interest (Figure 3).

Case		HS^- (mol L^{-1})	Mg^{2+} (mol L^{-1})	Cl^- (mol L^{-1})	SO_4^{2-} (mol L^{-1})	$O_{2(aq)}$ (mol L^{-1})	Fe^{2+} (mol L^{-1})
BASE	Max	5.1×10^{-3}	4.6×10^{-1}	6.2	4.2×10^{-2}	2.6×10^{-4}	4.2×10^{-4}
	Min	1.4×10^{-13}	4.7×10^{-4}	3.2×10^{-3}	1.2×10^{-7}	$^{*}1.8 \times 10^{-64}$	6.3×10^{-15}
S1	Max	5.1×10^{-3}	4.6×10^{-1}	6.2	4.2×10^{-2}	1.3×10^{-3}	4.2×10^{-4}
	Min	1.3×10^{-13}	5.7×10^{-4}	3.2×10^{-3}	1.7×10^{-7}	$^{*}1.8 \times 10^{-64}$	4.2×10^{-15}
S2	Max	1.1×10^{-2}	4.6×10^{-1}	6.2	4.2×10^{-2}	2.6×10^{-4}	4.2×10^{-4}
	Min	1.4×10^{-13}	4.7×10^{-4}	3.2×10^{-3}	6.7×10^{-10}	$^{*}1.8 \times 10^{-64}$	6.3×10^{-15}
S3	Max	5.0×10^{-3}	4.5×10^{-1}	6.2	4.2×10^{-2}	2.6×10^{-4}	4.2×10^{-4}
	Min	1.5×10^{-13}	4.0×10^{-4}	3.9×10^{-3}	1.3×10^{-7}	$^{*}1.8 \times 10^{-64}$	5.2×10^{-15}

*reflecting equilibrium with FeS.

five-fold, O_2 in meltwater does not provide a substantial control on redox conditions in the subsurface.

However, increasing the biogenic sulphate reduction rate by one order of magnitude (S2) results in higher average HS^- and lower SO_4^{2-} concentrations up to depths of 600 and 400 mbgs, respectively, in comparison to the BASE case (Figures 10(a) and 10(c)). The effect is muted, considering that the maximum average HS^- and SO_4^{2-} concentrations increase or, respectively, decrease two-fold, despite a change in reactivity by a factor of 10 (Figures 10(a) and 10(c)). Comparing these results to observations (Figure C-7) still shows a satisfactory fit, although simulated results for HS^- are at the higher end of the observed data. These results suggest that the rate of sulphate reduction is an important and relatively sensitive parameter in the control of the formation and fate of sulphidic waters, which is not surprising. Regrettably, this parameter is also quite difficult to quantify reliably.

Increasing the maximum thickness of the ice sheet from 2,000 to 3,000 m (S3) results in a deeper reach of elevated sulphide concentrations (Figure 10). This is likely due to the elevated hydraulic heads below the melting ice sheet during the deglaciation stage, resulting in steeper hydraulic gradients and deeper meltwater ingress. These results suggest that the ice sheet thickness and the associated hydraulic conditions during a glaciation-deglaciation cycle also deserve attention. The comparison of simulated results to observations (Figure C-8) is of very similar quality as the one for the reference case (BASE).

Table 2 provides a summary of the reference case (BASE) and the sensitivity analysis results, confirming that maximum and minimum for HS^- and SO_4^{2-} are not substantially affected for cases S1 and S3 relative to the reference case (BASE), while larger impacts can be seen for case S2. Impacts of parameter variations in the sensitivity analysis on other chemical elements are either negligible (Mg^{2+} and Cl^-) or modest ($O_{2(aq)}$, Fe^{2+}) (Table 2).

5. Conclusions

The temporal evolution and spatial distribution of sulphidic waters in a simplified 2D intracratonic sedimentary basin were investigated for a hypothetical 32,500-year glaciation-deglaciation cycle using reactive transport simulations. Simulated component concentration profiles from a subregion of the domain were qualitatively compared to observed data from the Michigan Basin. Overall, simulation results showed good agreement with observational data, after subjecting the model to a full glaciation-deglaciation cycle. The comparison is considered qualitative in nature because the conceptual model does not capture the detailed stratigraphic and lithological compositions of the Michigan Basin. In addition, parameterization of such a large-scale model is challenging.

Although the simulations were partially constrained by the structure and geometry of sedimentary basins in North America and related field observations, several assumptions and simplifications had to be made. The most important simplifying assumptions are related to material properties of different geological units, geochemical processes, distribution of component concentrations, and mineral abundance, as well as cold- and warm-based boundary conditions during ice sheet advancement and retreat. In addition, simplifications were made regarding the dimensionality (2D), neglecting the presence of fractures, mineral compositions of the rock units, and the rate expressions for sulphate reduction and mineral dissolution/precipitation reactions. These simplifications and assumptions lead to substantial uncertainties and thus limit the model's predictive capability.

Nevertheless, simulation results are valuable to delineate system behaviour and evolution, and aid in developing an understanding of the key processes leading to present-day hydrogen sulphide concentration distributions in the region of interest. Analysis of a reference case confirms that present-day elevated hydrogen sulphide concentrations observed at depths of around 100-200 mbgs are due to low $O_{2(aq)}$ concentrations and relatively low salinities in this depth range. The simulations indicate that consumption of $O_{2(aq)}$ occurs at very shallow depth related to organic matter decomposition and reductive dissolution reactions. In addition, simulations capture the inhibitive effect of elevated fluid salinity at greater depth on sulphate reduction. The

model also allowed to evaluate uncertainties of controlling factors related to elevated sulphide concentrations through a sensitivity analysis, highlighting the sensitivity of model results to the rate of sulphate reduction, a parameter that is not well constrained.

Simulation results indicate that geochemical conditions, including sulphur cycling in low-permeability limestone and dolostone units, remain unaffected during a glaciation-deglaciation cycle, even at shallow depths of 25 mbgs. The same is valid for shale units, which are characterized by even lower permeability and have an even larger redox buffer capacity. The results also suggest that geochemical conditions, including sulphide concentrations, below a depth of 500 mbgs remain relatively unaffected in all units over the entire glaciation-deglaciation cycle. These results speak to a high level of long-term geochemical stability at depths below 500 mbgs with relatively low sulphide concentrations due to the continuous presence of high salinity pore waters at and below this depth.

Data Availability

Field observational data are available in 2015-3: The Isotopic Characterization of Water in Paleozoic Bedrock Formations in Southwestern Ontario (http://www.ogsrlibrary.com/publications_index_ontario_oil_gas).

Conflicts of Interest

The authors declare that there are no conflicts of interest regarding the publication of this paper.

Acknowledgments

Supplementary Materials

Additional information can be found in the Supplementary Information, including the following: (A) Location of the profile A-B in Figure 1 in Southern Ontario, Canada, and additional field observation data. (B) Additional information on model setup and parameterization. (C) Additional simulation results. (*Supplementary Materials*)

References

[1] M. Y. Hobbs, S. K. Frape, O. Shouakar-Stash, and L. R. Kennell, *Regional Hydrogeochemistry-Southern Ontario. Nuclear Waste Management Organization*, Technical report NWMO DGR-TR-2011-12, 2011.

[2] T. R. Carter, D. Wang, A. Castillo, and L. Fortner, *Water Type Maps of Deep Groundwater from Petroleum Well Records, Southern Ontario*, Ontario Oil, Gas and Salt Resources Library, open file data release 2015-1, 10 p. 89 maps, 2015.

[3] T. R. Carter and L. Sutherland, *Mapping the Interface between the Intermediate Sulphur Water Regime and Deep Brine in the Paleozoic Bedrock of Southwestern Ontario*, Ontario Oil, Gas and Salt Resources Library, Open File Data Release 2018-2, 2018.

[4] E. P. Moldovanyi, L. M. Walter, and L. S. Land, "Strontium, boron, oxygen, and hydrogen isotope geochemistry of brines from basal strata of the Gulf Coast sedimentary basin, USA," *Geochimica et Cosmochimica Acta*, vol. 57, no. 9, pp. 2083–2099, 1993.

[5] S. Creaney and J. Allan, "Hydrocarbon generation and migration in the Western Canada sedimentary basin," *Geological Society, London, Special Publications*, vol. 50, no. 1, pp. 189–202, 1990.

[6] G. Zhu, S. Zhang, H. Huang, Y. Liang, S. Meng, and Y. Li, "Gas genetic type and origin of hydrogen sulfide in the Zhongba gas field of the western Sichuan Basin, China," *Applied Geochemistry*, vol. 26, no. 7, pp. 1261–1273, 2011.

[7] G. Etiope, G. Papatheodorou, D. P. Christodoulou, G. Ferentinos, E. Sokos, and P. Favali, "Methane and hydrogen sulfide seepage in the Northwest Peloponnesus petroliferous basin (Greece): origin and geohazard," *Bulletin*, vol. 90, no. 5, pp. 701–713, 2006.

[8] Q. Wang, "Generation mechanism and control measures for H2S in oil wells, Liaohe oilfield," *Petroleum Exploration and Development*, vol. 35, no. 3, pp. 349–354, 2008.

[9] R. A. Marriott, P. Pirzadeh, J. J. Marrugo-Hernandez, and S. Raval, "Hydrogen sulfide formation in oil and gas," *Canadian Journal of Chemistry*, vol. 94, no. 4, pp. 406–413, 2016.

[10] M. S. Wiener, B. V. Salas, M. Quintero-Núñez, and R. Zlatev, "Effect of H2S on corrosion in polluted waters: a review," *Corrosion Engineering, Science and Technology*, vol. 41, no. 3, pp. 221–227, 2006.

[11] S. Briggs, J. McKelvie, P. Keech, B. Sleep, and M. Krol, "Transient modelling of sulphide diffusion under conditions typical of a deep geological repository," *Corrosion Engineering, Science and Technology*, vol. 52, sup1, pp. 200–203, 2017.

[12] S. L. Malone Rubright, L. L. Pearce, and J. Peterson, "Environmental toxicology of hydrogen sulfide," *Nitric Oxide*, vol. 71, pp. 1–13, 2017.

[13] F. King, M. Kolar, and M. Vähänen, "Reactive-transport modelling of the sulphide-assisted corrosion of copper nuclear waste canisters," in *Sulphur-Assisted Corrosion in Nuclear Disposal Systems*, pp. 152–164, Maney Publishing Leeds, United Kingdom, 2011.

[14] M. Pekala, P. Wersin, V. Cloet, and N. Diomidis, "Reactive transport calculations to evaluate sulphide fluxes in the near-field of a SF/HLW repository in the Opalinus clay," *Applied Geochemistry*, vol. 100, pp. 169–180, 2019.

[15] M. Pekala, P. Smith, P. Wersin, N. Diomidis, and V. Cloet, "Comparison of models to evaluate microbial sulphide generation and transport in the near field of a SF/HLW repository in Opalinus clay," *Journal of Contaminant Hydrology*, vol. 228, p. 103561, 2020.

[16] P. De Cannière, B. Kursten, F. Druyts, H. Moors, and R. Gens, "Sulphur-related issues in deep underground nuclear waste

disposal systems," in *Sulphur-Assisted Corrosion In Nuclear Disposal Systems*, pp. 165–169, CRC press, 2020.

[17] D. S. Hall, M. Behazin, W. Jeffrey Binns, and P. G. Keech, "An evaluation of corrosion processes affecting copper-coated nuclear waste containers in a deep geological repository," *Progress in Materials Science*, vol. 118, p. 100766, 2021.

[18] J. W. Morse, F. J. Millero, J. C. Cornwell, and D. Rickard, "The chemistry of the hydrogen sulfide and iron sulfide systems in natural waters," *Earth-Science Reviews*, vol. 24, no. 1, pp. 1–42, 1987.

[19] A. M. Sharrar, B. E. Flood, J. V. Bailey et al., "Novel large sulfur bacteria in the metagenomes of groundwater-fed chemosynthetic microbial mats in the Lake Huron basin," *Frontiers in Microbiology*, vol. 8, p. 791, 2017.

[20] B. A. An, Y. Shen, and G. Voordouw, "Control of sulfide production in high salinity Bakken shale oil reservoirs by halophilic bacteria reducing nitrate to nitrite," *Frontiers in Microbiology*, vol. 8, p. 1164, 2017.

[21] J. Herrero, O. Artieda, and W. h. Hudnall, "Gypsum, a tricky material," *Soil Science Society of America Journal*, vol. 73, no. 6, pp. 1757–1763, 2009.

[22] P. Pitkaenen, S. Partamies, and A. Luukkonen, *Hydrogeochemical Interpretation of Baseline Groundwater Conditions at the Olkiluoto Site*, Technical report POSIVA–03-07, 2004.

[23] S. A. Bea, D. Su, K. U. Mayer, and K. T. B. MacQuarrie, "Evaluation of the potential for dissolved oxygen ingress into deep sedimentary basins during a glaciation event," *Geofluids*, vol. 2018, Article ID 9475741, 20 pages, 2018.

[24] M. Gascoyne, "Evolution of redox conditions and groundwater composition in recharge-discharge environments on the Canadian shield," *Hydrogeology Journal*, vol. 5, no. 3, pp. 4–18, 1997.

[25] J. C. McIntosh, G. Garven, and J. S. Hanor, "Impacts of Pleistocene glaciation on large-scale groundwater flow and salinity in the Michigan Basin," *Geofluids*, vol. 11, no. 1, pp. 18–33, 2011.

[26] J. C. McIntosh, L. M. Walter, and A. M. Martini, "Pleistocene recharge to midcontinent basins: effects on salinity structure and microbial gas generation," *Geochimica et Cosmochimica Acta*, vol. 66, no. 10, pp. 1681–1700, 2002.

[27] J. C. McIntosh and L. M. Walter, "Volumetrically significant recharge of Pleistocene glacial meltwaters into epicratonic basins: constraints imposed by solute mass balances," *Chemical Geology*, vol. 222, no. 3-4, pp. 292–309, 2005.

[28] S. A. Bea, K. U. Mayer, and K. T. B. MacQuarrie, "Modelling reactive transport in sedimentary rock environments, phase II: MIN3P code enhancements and illustrative simulations for a glaciation scenario," *Nuclear Waste Management Organization*, Technical report NWMO-TR-2011-13, 2011.

[29] S. A. Bea, U. K. Mayer, and K. T. B. MacQuarrie, "Reactive transport and thermo-hydro-mechanical coupling in deep sedimentary basins affected by glaciation cycles: model development, verification, and illustrative example," *Geofluids*, vol. 16, no. 2, pp. 279–300, 2016.

[30] M. Xie, D. Su, K. U. Mayer, and K. T. B. MacQuarrie, "Reactive transport modelling investigation of elevated dissolved sulphide concentrations in sedimentary basin rocks," *Nuclear Waste Management Organization*, Technical report NWMO-TR-2011-13, 2018.

[31] K. U. Mayer, E. O. Frind, and D. W. Blowes, "Multicomponent reactive transport modeling in variably saturated porous media using a generalized formulation for kinetically con-trolled reactions," *Water Resources Research*, vol. 38, no. 9, pp. 13-1–13-21, 2002.

[32] T. R. Carter, F. R. Brunton, J. K. Clark et al., *A Three-Dimensional Geological Model of the Paleozoic Bedrock of Southern Ontario*, Geological Survey of Canada, Open File 8618, 2019.

[33] K. K. Brandt, F. Vester, A. N. Jensen, and K. Ingvorsen, "Sulfate reduction dynamics and enumeration of sulfate-reducing bacteria in hypersaline sediments of the Great Salt Lake (Utah, USA)," *Microbial Ecology*, vol. 41, no. 1, pp. 1–11, 2001.

[34] D. Littlewood and J. R. Postgate, "Sodium chloride and the growth of Desulphovibrio desulphuricans," *Journal of General Microbiology*, vol. 17, no. 2, pp. 378–389, 1957.

[35] A. Oren, "Bioenergetic aspects of halophilism," *Microbiology and Molecular Biology Reviews*, vol. 63, no. 2, pp. 334–348, 1999.

[36] M. Foti, D. Y. Sorokin, B. Lomans et al., "Diversity, activity, and abundance of sulfate-reducing bacteria in saline and hypersaline soda Lakes," *Applied and Environmental Microbiology*, vol. 73, no. 7, pp. 2093–2100, 2007.

[37] M. Skuce, *Isotopic Fingerprinting of Shallow and Deep Groundwaters in Southwestern Ontario and Its Applications to Abandoned Well Remediation*, The University of Western Ontario. Electronic thesis and dissertation repository, 2014.

[38] M. Skuce, F. J. Longstaffe, T. R. Carter, and J. Potter, "Isotopic fingerprinting of groundwaters in southwestern Ontario: applications to abandoned well remediation," *Applied Geochemistry*, vol. 58, pp. 1–13, 2015.

[39] M. Person, J. McIntosh, V. Bense, and V. H. Remenda, "Pleistocene hydrology of North America: the role of ice sheets in reorganizing groundwater flow systems," *Reviews of Geophysics*, vol. 45, no. 3, 2007.

[40] D. Su, M. Xie, K. U. Mayer, and K. T. B. MacQuarrie, "The impact of ice sheet geometry on meltwater ingress and reactive solute transport in sedimentary basins," *Water Resources Research*, vol. 58, no. 10, 2022.

[41] G. K. C. Clarke, S. G. Collins, and D. E. Thompson, "Flow, thermal structure, and subglacial conditions of a surge-type glacier," *Canadian Journal of Earth Sciences*, vol. 21, no. 2, pp. 232–240, 1984.

[42] J. A. MacGregor, M. A. Fahnestock, G. A. Catania et al., "A synthesis of the basal thermal state of the Greenland ice sheet," *JGR Earth Surface*, vol. 121, no. 7, pp. 1328–1350, 2016.

[43] R. I. Waller, "The influence of basal processes on the dynamic behaviour of cold-based glaciers," *Quaternary International*, vol. 86, no. 1, pp. 117–128, 2001.

[44] C. Pickler, H. Beltrami, and J.-C. Mareschal, "Laurentide ice sheet basal temperatures during the last glacial cycle as inferred from borehole data," *Climate of the Past*, vol. 12, no. 1, pp. 115–127, 2016.

[45] A. M. Provost, C. I. Voss, and C. E. Neuzil, "Glaciation and regional groundwater flow in the Fennoscandian shield," *Geofluids*, vol. 12, no. 1, pp. 79–96, 2012.

[46] H. G. Machel, "Bacterial and thermochemical sulfate reduction in diagenetic settings – old and new insights," *Sedimentary Geology*, vol. 140, no. 1-2, pp. 143–175, 2001.

[47] M. A. M. Reis, J. S. Almeida, P. C. Lemos, and M. J. T. Carrondo, "Effect of hydrogen sulfide on growth of sulfate reducing bacteria," *Biotechnology and Bioengineering*, vol. 40, no. 5, pp. 593–600, 1992.

[48] S. Moosa, M. Nemati, and S. T. L. Harrison, "A kinetic study on anaerobic reduction of sulphate, part I: effect of sulphate concentration," *Chemical Engineering Science*, vol. 57, no. 14, pp. 2773–2780, 2002.

[49] S. Sudarno, N. Hardyanti, K. Serafina, and A. Oktaviana, "Effect of iron and manganese concentration on the sulfate reducing process in acid mine drainage," *Journal of Physics: Conference Series*, vol. 1295, no. 1, article 012060, 2019.

[50] J. W. H. Oude Elferink Stefanie, A. Visser, L. W. Hulshoff Pol, and A. J. M. Stams, "Sulfate reduction in methanogenic bioreactors," *FEMS Microbiology Reviews*, vol. 15, no. 2–3, pp. 119–136, 1994.

[51] Quintessa Ltd, and Geofirma Engineering Ltd, *Postclosure Safety Assessment: Data. Nuclear Waste Management Organization*, Technical report NWMO DGR-TR-2011-25, 2011.

[52] F. P. de França, C. A. Ferreira, and M. T. S. Lutterbach, "Effect of different salinities of a dynamic water system on biofilm formation," *Journal of Industrial Microbiology & Biotechnology*, vol. 25, no. 1, pp. 45–48, 2000.